remote sensing

IMPACT FACTOR 4.2

CITESCORE 8.3

Article

Multiple-Input Multiple-Output Microwave Tomographic Imaging for Distributed Photonic Radar Network

Carlo Noviello, Salvatore Maresca, Gianluca Gennarelli, Antonio Malacarne, Filippo Scotti, Paolo Ghelfi, Francesco Soldovieri, Ilaria Catapano and Rosa Scapaticci

Special Issue

State-of-the-Art and Future Developments: Short-Range Radar

Edited by

Dr. Yanhua Wang, Dr. Liang Zhang, Dr. Shunqiao Sun and Dr. Pu Wang

MDPI

https://doi.org/10.3390/rs16213940

remote sensing

MDPI

Article

Multiple-Input Multiple-Output Microwave Tomographic Imaging for Distributed Photonic Radar Network

Carlo Noviello [1,*], Salvatore Maresca [2], Gianluca Gennarelli [1], Antonio Malacarne [3], Filippo Scotti [3], Paolo Ghelfi [3], Francesco Soldovieri [1], Ilaria Catapano [1] and Rosa Scapaticci [1]

[1] Institute for Electromagnetic Sensing of the Environment (IREA), National Research Council (CNR), 80124 Napoli, Italy; gennarelli.g@irea.cnr.it (G.G.); soldovieri.f@irea.cnr.it (F.S.); catapano.i@irea.cnr.it (I.C.); scapaticci.r@irea.cnr.it (R.S.)

[2] Institute of Electronics and Information Engineering and Telecommunications (IEIIT), National Research Council (CNR), 56124 Pisa, Italy; salvatore.maresca@cnr.it

[3] Photonic Networks & Technologies National Laboratory (PNTLab), National Inter-University Consortium for Telecommunications (CNIT), 56124 Pisa, Italy; antonio.malacarne@cnit.it (A.M.); filippo.scotti@cnit.it (F.S.); paolo.ghelfi@cnit.it (P.G.)

* Correspondence: noviello.c@irea.cnr.it; Tel.: +39-0817620656

Abstract: This paper deals with the imaging problem from data collected by means of a microwave photonics-based distributed radar network. The radar network is leveraged on a centralized architecture, which is composed of one central unit (CU) and two transmitting and receiving dual-band remote radar peripherals (RPs), it is capable of collecting monostatic and multistatic phase-coherent data. The imaging is herein formulated as a linear inverse scattering problem and solved in a regularized way through the truncated singular value decomposition inversion scheme. Specifically, two different imaging schemes based on an incoherent fusion of the tomographic images or a fully coherent data processing are herein developed and compared. Experimental tests carried out in a port scenario for imaging both a stationary and a moving target are reported to validate the imaging approach.

Keywords: microwave tomography; microwave photonics; MIMO radar imaging; photonic radar network; coherent MIMO

check for updates

Citation: Noviello, C.; Maresca, S.; Gennarelli, G.; Malacarne, A.; Scotti, F.; Ghelfi, P.; Soldovieri, F.; Catapano, I.; Scapaticci, R. Multiple-Input Multiple-Output Microwave Tomographic Imaging for Distributed Photonic Radar Network. *Remote Sens.* **2024**, *16*, 3940. https://doi.org/10.3390/rs16213940

Academic Editors: Yanhua Wang, Liang Zhang, Shunqiao Sun and Pu Wang

Received: 11 September 2024
Revised: 19 October 2024
Accepted: 21 October 2024
Published: 23 October 2024

Copyright: © 2024 by the authors. Licensee MDPI, Basel, Switzerland. This article is an open access article distributed under the terms and conditions of the Creative Commons Attribution (CC BY) license (https://creativecommons.org/licenses/by/4.0/).

1. Introduction

Multiple-input Multiple-Output (MIMO) radars are an innovative sensing technology that is attracting huge attention among the scientific community and industries [1]. Different from standard monostatic phased-array radars, MIMO radars are based on the transmission of multiple probing signals [2] through different antennas and the simultaneous reception of the backscattered signals with multiple receiving antennas. MIMO radars are grouped in co-located [3] and widely distributed antenna systems [4]. Co-located MIMO systems consist of TX and RX antennas physically located in the same space. MIMO radars with separated antennas, thanks to their geometric diversity, possess more degrees of freedom compared with co-located systems, thus providing enhanced performance in terms of detection, parameter estimation, imaging, clutter and jamming mitigation, etc. [4]. As well known, the range resolution of standard monostatic radars (one TX and one RX co-located antenna) depends on the transmitted signal bandwidth whereas the cross-range resolution is related to the antenna beamwidth [5]. However, monostatic systems can estimate only the radial component of the target velocity from the Doppler shift induced by the relative motion between the target and radar. Conversely, MIMO radar systems, by employing multiple spatially distributed antennas, have several peculiarities; for example, (i) they are more robust with respect to stealthy targets, (ii) allow the obtaining of high resolution images along cross-range coordinates, and (iii) are capable of estimating

different targets' velocity components [3], thus leading to a more accurate reconstruction of the targets' trajectory and kinematics. Therefore, thanks to these important features, widely distributed systems may be profitably exploited in different security contexts, e.g., automotive applications, infrastructure monitoring, border security, cultural heritage, and environmental monitoring.

MIMO radar networks may be implemented by adopting decentralized or centralized approaches. Decentralized MIMO radars consist of multisite sensors, which operate as independent systems: each radar node acts as a standalone unit, and it performs a local processing on the received signals. The processed information is then transmitted to a central unit (CU), which performs a data fusion procedure [6]. On the other hand, in a centralized MIMO radar paradigm, the whole data processing is carried out at the CU. The centralized processing architecture potentially provides better performance, but at the same time, it requires a high level of time and phase coherence, guaranteed by the CU management [6].

Although many MIMO radar system technologies have been recently investigated, e.g., vector array MIMO radars (or EMVS-MIMO radars) [7], conformal array MIMO radars [8,9], and IRS-aided MIMO radars [10], hereafter, we focus on widely distributed MIMO radar systems currently operating in real scenarios. Indeed, to the best of the authors' knowledge, only a few spatially distributed multistatic radars have been tested in operative environments [11–21]. For instance, the prototype system named NeXtRAD has been proposed in [11–16]. NeXtRAD is an X-band radar network composed of one transmitter (TX) and three receivers (RX) widely distributed antennas operating at a short range of up to 1 km.

The MIRA-CLE MIMO radar system, operating at X- and Ka-bands, was then proposed in [17,18]. In particular, the X-band sensor is composed of 16 TX and 14 RX co-located antennas working at 9.45 GHz with a bandwidth of 1 GHz, while the Ka-band sensor has 8 TX and 16 RX co-located antennas operating at 36.22 GHz with a 400 MHz bandwidth. The maximum range coverage is about 600 m and 150 m for X- and Ka-band systems, respectively.

The Melissa MIMO system, presented in 2013, is a MIMO ground-based SAR system composed of 12 TX and 12 RX separated antennas operating at 13.3 GHz with a maximum coverage of 150 m [19].

A MIMO radar system, for small drone detection purposes, has been recently proposed in [20]. This system is made up of 6 TX and 6 RX co-located antennas operating at a carrier frequency of 3.3 GHz and with 6 km range coverage.

More recently, a new generation of MIMO radars based on microwave photonics (MWP) technology has been introduced [21]. Such a technology exploits optical fibers for distributing optical signals across the radar nodes with negligible additional phase noise [22], thus enabling centralized generation of extremely stable radar signals while guaranteeing phase coherence among them. Compared to RF MIMO systems, MWP MIMO radars can operate simultaneously in multiple frequency bands ensuring insensitivity to electromagnetic interference. Thanks to these peculiar features, MWP is paving the way to the development of innovative widely distributed MIMO radars under a fully centralized processing paradigm. As a matter of fact, in two recent EU-funded projects, i.e., RANGER [23] and ROBORDER [24], two MWP MIMO radar architectures have been proposed in the fields of maritime border security and search-and-rescue (SaR) operations. The photonic MIMO system proposed in [21] is composed of 3 TXs and 3 RXs operating at S- and X-bands and widely separated from each other and connected to a CU via fiber optic links.

In this work, we focus our attention on the distributed photonic radar network, earlier described in [21] and currently operating in the port of Livorno, Italy. Specifically, in this paper, an imaging algorithm based on microwave tomography (MWT) [25,26] is proposed to fully exploit the potentialities of the MWP distributed radar network [21]. Indeed, thanks to its flexibility in handling different measurement configurations and scenarios

(e.g., see [26–31]), MWT is shown to be an effective processing approach for data collected by distributed MWP radar systems. The proposed imaging technique is here referred to as MIMO microwave tomography (MIMO-MWT). The MIMO-MWT approach is based on the solution of an electromagnetic inverse scattering problem, which is here formulated under the linear Born model [32]. Furthermore, the data inversion is carried out in a regularized way by exploiting the well-known method, truncated singular-value decomposition (TSVD) [33,34]. This method ensures a reliable and stable solution, with respect to the noise, of the inverse scattering problem while providing a smoothed reconstruction of the target [33]. The MIMO-MWT approach is herein validated by processing real data collected during a measurement campaign performed at Livorno harbor, Italy.

This paper is organized as follows. Section 2 describes the MIMO radar system architecture, while Section 3 reports the signal processing methodology based on the MIMO-MWT approach. The experimental validation of the MIMO-MWT imaging approach is reported in Section 4. A final discussion on the achieved results and concluding remarks follow in Section 5.

2. Description of MIMO Radar Systems

The original design of the MIMO radar network architecture was based on a CU and three remoted radar peripherals (RPs), acting as transceivers (i.e., TX/RX) for a total of nine physical channels [21]. The master oscillator at the CU is a mode-locked laser (MLL), whose output spectrum is a coherent optical frequency comb with a frequency spacing of f_{MLL} = 400 MHz. By splitting this optical signal using an arrayed waveguide grating (AWG), it is possible to spatially separate two spectral portions of optical modes for each RP. One of them is employed for the optical-to-electrical (O/E) conversion of the electrical radar waveform distributed to the RPs, whereas the other is used for the electrical-to-optical (E/O) conversion of the received target echoes at the RPs that are sent back to the CU through optical fiber links. This solution allows the system to potentially select any of the best products at frequencies of $f_{\mathrm{RF}} = k \cdot f_{\mathrm{MLL}} + f_{\mathrm{IF}}$, where f_{RF} is the carrier radio frequency (RF), f_{IF} is the intermediate frequency (IF), and k is an integer number. In the proposed system, the radar waveform replica at 2.9 and 9.7 GHz, corresponding to k = 7 and k = 24, respectively, where f_{IF} = 100 MHz, are selected by an electrical filter, amplified, and transmitted by the S-band and X-band antennas including front-ends dedicated to each operation band. Further information about signal generation and reception can be found in [21].

However, at present, due to technical field impairments, only two TX/RX radar peripherals are fully operative, as shown in Figure 1. This determines a degradation of the achievable performance due to a global coverage reduction in the monitored area and a limitation of the data angular diversity.

The two radar peripherals RP1 and RP2 are highlighted in green and yellow, respectively, and superimposed on a satellite image of the site, taken from Google Earth. The radar configuration allows covering a common area with some angular diversity with a corresponding bistatic angle of about 40°. More details about the MIMO radar installation on the Livorno harbor site can be found in [21].

The monitored area is modeled as a 3D Cartesian observation space, where a generic point (x, y, and z) denotes the East, North, and Up (ENU) local coordinates referring to the origin, fixed in correspondence to RP1. As already mentioned, each RP is equipped with an S-band and an X-band horn antenna, which are typically deployed in maritime surveillance scenarios. The horn antennas for the two employed carriers are compact, are easily deployable, and are characterized by approximately 20 dBi gain and 18° half-power beamwidth (HPBW) aperture.

Figure 1. Radar network configuration at Livorno harbor, Italy. RP1 and RP2 indicate the locations of the active radar peripherals. The green and yellow triangles represent, approximately, the antenna viewing angles.

The radar network architecture implements a transmission scheme based on time-division multiplexing, described as follows. When RP1 transmits the S-band waveform, RP2 is silent; then, both RPs record the received echoes. Subsequently, RP1 transmits the X-band waveform, and the RPs record the radar echoes. Afterwards, RP2 transmits and the former scheme repeats, in a round-robin fashion, thus leading to an interleaved data stream. This scheme assures that signals associated to different frequency bands and different TX/Rx radar couples, i.e. different channels, do not interfere one to each other. The main operative radar system parameters are summarized in Table 1.

Table 1. Radar Network System Parameters.

	Parameter	Description/Value
RP1	Latitude	43°33′12.24″N
	Longitude	10°17′51.89″E
	Altitude	5 m
RP2	Latitude	43°33′12.24″N
	Longitude	10°17′51.89″E
	Altitude	5 m
	Waveform	Linear-frequency-modulated chirp
	Pulse duration	2 μs
	S-band carrier frequency	2.9 GHz
	X-band carrier frequency	9.7 GHz
	Operative bandwidth	100 MHz
	Pulse repetition frequency	20 kHz
	Sampling frequency	400 MHz
	No. of TXs/RXs (channels)	2 × 2 (2 monostatic, 2 bistatic)

3. Signal Processing Procedure

This section reports the steps and tools used to process the raw radar data in order to provide the final focused image of the target of interest. The overall signal processing procedure is reported in Figure 2, where it is possible to identify a pipeline consisting of

two stages: (1) pre-processing and (2) focusing, which is based on the MWT approach, as better detailed in the following subsections.

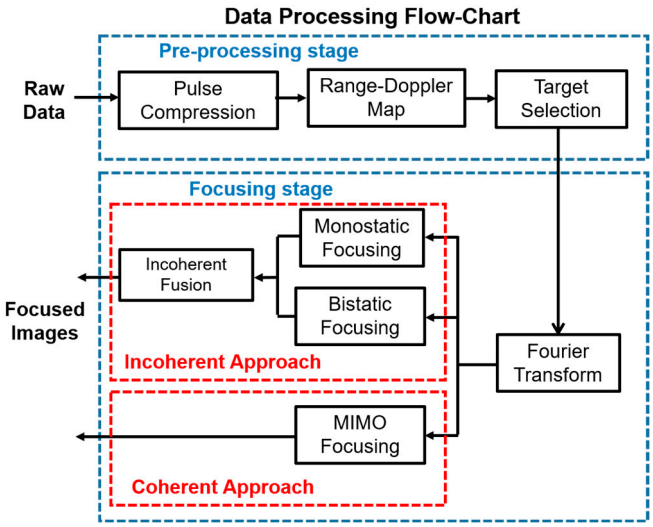

Figure 2. Block diagram of the signal processing pipeline.

3.1. Pre-Processing Stage

In the pre-processing stage, the raw data on each of the four radar channels undergo a standard pulse compression, which cross-correlates the received signals with the reference transmitted signal. In this way, it is possible to enhance the range resolution and the signal-to-noise ratio [35]. The resulting data are then transformed into the range–Doppler (RD) domain by the Fast Fourier Transform (FFT) algorithm. This operation, based on the Doppler effect [35], is crucial for discriminating the signal contributions coming from moving and static targets. In this respect, for the sake of clarity, Figure 3 shows an example of an RD map relevant to a field test. As can be seen, the static targets are concentrated at the zero-Doppler frequency; conversely, the signatures of the moving targets are shifted along the Doppler direction with respect to the static targets. Accordingly, the signals—due to static targets—are deleted by filtering out the zero-Doppler frequency components.

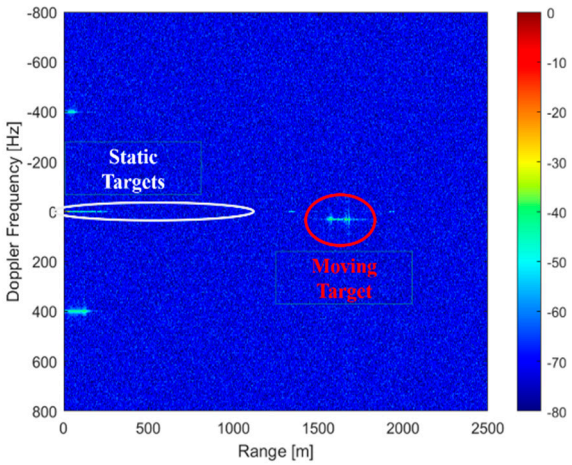

Figure 3. A range–Doppler map related to an experimental test. The white and red ellipses show the contributions from static and moving targets, respectively.

After RD processing, the signal components related to the target to be imaged are selected by means of a cropping procedure [36]. The cropping extracts the radar traces associated with the target over each channel, and consequently, it filters out the signal contributions due to other targets and unwanted clutter. Once the target of interest has

been selected, the radar data in the fast-time domain (range profiles) are converted into the frequency domain through an FFT. This processing step is necessary because the focusing algorithm, as detailed in the following subsection, acts on frequency domain data.

3.2. MWT Focusing Stage

The inversion strategy, providing a focused image of the scene from the data as coming from the pre-processing stage, is based on the microwave tomographic approach described herein.

Let us refer to the 2D scenario sketched in Figure 4. Here, the two radars RP1 and RP2 probe the investigation domain D where the targets are supposed to be located. We denote with $\boldsymbol{r}_m^{tx}$ and $\boldsymbol{r}_n^{rx}$ the positions of the transmitting and receiving antennas, respectively, that are modeled for simplicity as 2D electric line sources directed along z (TM polarization) and operating in the angular frequency band $\Omega = [\omega_{min}, \omega_{max}]$. The indexes (m, n) vary over the set $\{1, 2\}$, thus defining the four radar channels, i.e.,

$$\begin{cases} m = 1,\ n = 1 & \text{monostatic RP1} \\ m = 1,\ n = 2 & \text{bistatic RP1} - \text{RP2} \\ m = 2,\ n = 1 & \text{bistatic RP2} - \text{RP1} \\ m = 2, n = 2 & \text{monostatic RP2} \end{cases} \tag{1}$$

A free-space scenario is assumed where the presence of targets in D is described by the contrast function $\chi(\boldsymbol{r}) = \varepsilon_{rt}(\boldsymbol{r}) - 1$, where ε_{rt} is the target relative permittivity function at a generic point $\boldsymbol{r}$ in D. Note that χ accounts for the difference between the electromagnetic properties (dielectric permittivity and electrical conductivity) of the targets and those of the free space. The $e^{j\omega t}$ time dependence factor is assumed and omitted.

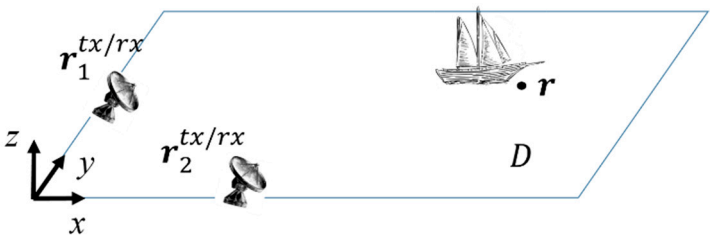

Figure 4. Geometry of the radar imaging problem.

The imaging is formulated by considering a linear model of the electromagnetic scattering based on the Born approximation [32]. For a single radar channel (m, n), i.e., $\boldsymbol{r}_m^{tx}$ and $\boldsymbol{r}_n^{rx}$ fixed, the measured scattered field $E^s\left(\boldsymbol{r}_m^{tx}, \boldsymbol{r}_n^{rx}, \omega\right)$ at the angular frequency $\omega \in \Omega$ is related to the unknown contrast function by the linear integral equation:

$$E^s\left(\boldsymbol{r}_m^{tx}, \boldsymbol{r}_n^{rx}, \omega\right) \approx \iint_D \frac{e^{-jk|\boldsymbol{r}_m^{tx} - \boldsymbol{r}|} e^{-jk|\boldsymbol{r}_n^{rx} - \boldsymbol{r}|}}{\sqrt{|\boldsymbol{r}_m^{tx} - \boldsymbol{r}||\boldsymbol{r}_n^{rx} - \boldsymbol{r}|}} \chi(\boldsymbol{r}) d\boldsymbol{r} = \mathcal{L}_{(m,n)}\chi \tag{2}$$

where $\mathcal{L}_{(m,n)} : L^2(D) \to L^2(\Omega)$ is a linear projection operator mapping χ in the data space referring to the channel (m, n).

Due to the compactness of the operator $\mathcal{L}_{(m,n)}$, the inversion of Equation (2) is an ill-posed problem [33]. Therefore, the application of a regularization scheme is mandatory for achieving a physically meaningful solution in the presence of data affected by noise. To achieve this goal, the TSVD inverse scheme is used in this work. In detail, $\{\sigma_p, u_p, v_p\}_{p=1}^{\infty}$ denotes the singular spectrum (the singular spectrum $\{\sigma_p, u_p, v_p\}_{p=1}^{\infty}$ varies with the radar channel (m, n), but such a dependence is skipped here to simplify the notation) of the operator $\mathcal{L}_{m,n}$, where σ_p is a singular value, and u_p and v_p are the orthonormal basis

functions in the data and unknown spaces, respectively. Then, the TSVD-based regularized solution to the inverse problem in Equation (2) can be written as [33] follows:

$$\widetilde{\chi}_{(m,n)}(\boldsymbol{r}) = \sum_{p=1}^{\overline{P}} \frac{\left\langle E^s\left(\boldsymbol{r}_m^{tx}, \boldsymbol{r}_n^{rx}, \omega\right),\ u_p \right\rangle}{\sigma_p} v_p(\boldsymbol{r}) \tag{3}$$

In Equation (3), $\langle\ ,\rangle$ is the inner product in the space of data, and $\overline{P}$ is the TSVD regularization parameter chosen to ensure a good trade-off in terms of stability and accuracy of the solution. A detailed and exhaustive description of TSVD scheme can be found in [33].

The amplitude of the retrieved complex contrast in Equation (3) defines the tomographic image $I_{(m,n)}$, referred to as a tomographic image.

With reference to Figure 2, depending on which channels are considered in the scattering model of Equation (2), one can refer to monostatic focusing if only monostatic data are considered; bistatic focusing if only bistatic contributions are selected; and MIMO focusing if all the four channels are considered simultaneously. In the former cases, an incoherent focusing strategy is adopted, based on the fusion of the tomographic reconstructions obtained for the different channels. For MIMO focusing, instead, a coherent focusing strategy is applied. In the following, both approaches are described in detail.

3.2.1. Incoherent Focusing

Based on TSVD inversion (see Equation (3)), a tomographic image $I_{(m,n)}$ is produced for each radar channel (m, n), and so, a set of four tomographic images is obtained (see Equation (1)). Each image is characterized by satisfactory focusing along the (mono-/bi-static) range due to the system bandwidth, but a poor angular resolution arises because only a single TX/RX pair is considered. Furthermore, the target is imaged at the same location on every channel. Accordingly, to gain some angular resolution, an image fusion strategy is implemented based on a pixel-wise multiplication of the images corresponding to each radar channel, i.e.,

$$I^{inch}(\boldsymbol{r}) = \prod_{m=1}^{2} \prod_{n=1}^{2} I_{(m,n)}(\boldsymbol{r}) \tag{4}$$

Note that the multiplicative fusion helps in emphasizing the target response and mitigating unwanted clutter due to the significant sidelobes associated with the target response (e.g., see [37]).

It is worth pointing out that the term "incoherent", adopted here and in the following, has nothing that relates with the phase coherence of the gathered MIMO signals. In fact, as all four available channels are used, the requirement on the phase coherence still holds true.

3.2.2. Coherent Focusing

The coherent strategy fully exploits the MIMO concept since it aims at producing a focused image of the scene by simultaneously inverting the scattered field data recorded over each radar channel. More specifically, if the TX and RX positions are allowed to vary according to Equation (1), then the integral equation to be inverted can be written as

$$E^s\left(\boldsymbol{r}_m^{tx}, \boldsymbol{r}_n^{rx}, \omega\right) \approx \iint_D \frac{e^{-jk|\boldsymbol{r}_m^{tx}-\boldsymbol{r}|} e^{-jk|\boldsymbol{r}_n^{rx}-\boldsymbol{r}|}}{\sqrt{|\boldsymbol{r}_m^{tx}-\boldsymbol{r}||\boldsymbol{r}_n^{rx}-\boldsymbol{r}|}} \chi(\boldsymbol{r}) d\boldsymbol{r} = \mathcal{L}\chi \tag{5}$$

where $\mathcal{L} : L^2(D) \rightarrow L^2\left(\boldsymbol{r}_m^{tx} \times \boldsymbol{r}_n^{rx} \times \Omega\right)$ is the operator mapping the unknown into the data space relevant to all the four radar channels.

The amplitude of the contrast map obtained through the inversion of Equation (5) via TSVD provides the focused tomographic image $I^{ch}(\boldsymbol{r})$.

4. Experimental Validation

The experimental analysis presented herein aims, from one side, to assess the imaging capability of the MWP radar network currently operating at the Livorno harbor, Italy, and, on the other side, to verify the effectiveness of the MIMO-MWT strategies, described in Section 3, for port monitoring purposes.

The dataset was acquired with the radar configuration previously described in Section 2. Unfortunately, the electronic components related to the X-band channels experienced some malfunctions that corrupted the X-band data. Therefore, only S-band data are considered to validate the data processing approach and compare the MWT focusing strategies. Note that, thanks to the radar network architecture, the issues regarding the X-band data do not affect the S-band data.

The dataset under consideration refers to a measurement campaign carried out on 23 July 2021, and it is composed of eight data frames manually recorded between 11:01:00 AM and 11:03:01 AM local time (see Table 2). Each frame comprises a number of 330 pulses that unadergo range–Doppler (RD) processing, as seen Figure 2. As an example, Figure 5 shows the pre-processed data in the RD domain relevant to Acquisition 1 for each radar channel (RP1-RP1 (a), RP1-RP2 (b), RP2-RP1 (c), and RP2-RP2 (d)). Apparently, in all the channels, the static objects can be easily distinguished from the moving targets. Note that the vertical axis of Figure 5 represents the radial speed, which is the projection of the vector representing the velocity of the target along the radar line of sight. This physical quantity is evaluated by exploiting the mathematical relation between the Doppler frequency, f_d, and the radial velocity, $v_r = \left(\frac{\lambda}{2\pi}\right) f_d$.

Table 2. Data Frame Acquisition.

Acquisition No.	Local Time
1	11:01:00 AM
2	11:01:34 AM
3	11:01:45 AM
4	11:01:52 AM
5	11:01:58 AM
6	11:02:05 AM
7	11:02:55 AM
8	11:03:01 AM

As regards the static objects, we focus the analysis on the lighthouse located at the end of the curvilinear dam bounding the entrance into the harbor (see Figure 6a). Note that the selection of the lighthouse signal contribution via the cropping procedure has been performed by assuming that (1) the lighthouse is the main scattering static target in the scene; (2) its monostatic and bistatic ranges over the four channels are known a priori; and (3) its Doppler contribution is fully concentrated around the zero-Doppler interval. As for the moving targets, at the time of the measurement campaign, it was possible to monitor the departure of a Grimaldi Lines ferryboat (Cruise Sardegna by Grimaldi Lines; see Figure 6b). This ferryboat regularly leaves the port of Livorno every day during the testing time interval. The Cruise Sardegna Grimaldi ferryboat has a length of 225 m and a width of approximately 31 for a tonnage of 54,310 tons. As shown in Figure 6b, the ship is a passenger ferry, and its daily route is depicted by the white curvilinear trajectory. The ferryboat route was charted by exploiting Google Earth PRO (v. 7.3.6.9796).

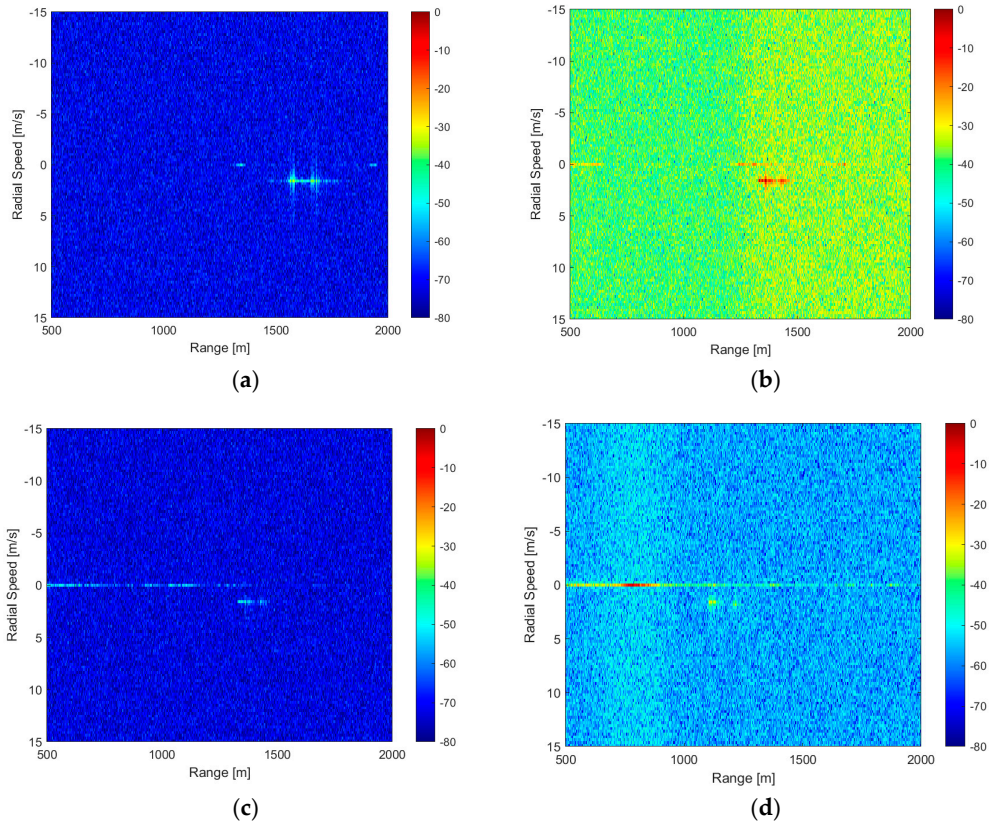

Figure 5. RD maps (normalized amplitude in dB) for each radar channel and Acquisition 1: RP1-RP1 (**a**), RP1-RP2 (**b**), RP2-RP1 (**c**), RP2-RP2 (**d**).

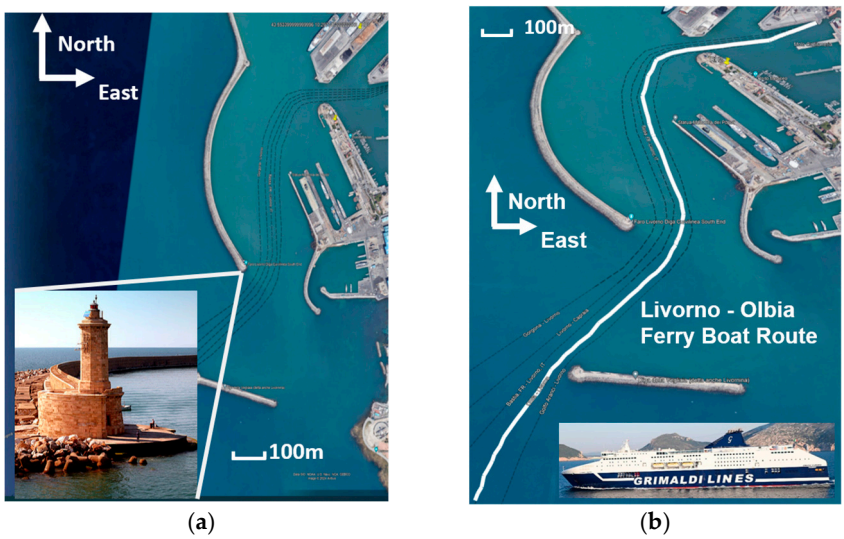

Figure 6. Pictures of the target under test: picture of the lighthouse representing the main scattering static object in the observed scene (**a**); picture of the Cruise Sardegna ferry and its daily route in the harbor represented by the white line (source: Google Earth) (**b**).

Thanks to its huge RCS and the a priori knowledge of its maritime route, this target was easily distinguishable from the other boats, thus representing a key target to be detected.

After the cropping of static or moving targets on the RD map, the related radar traces are selected and Fourier-transformed in the bandwidth [2.85, 2.95] GHz with a step of 85 KHz. Finally, MIMO-MWT data processing is applied by considering a TSVD truncation

index $\overline{P}$ such that singular values lower than 15 dB compared with the maximum one are neglected.

The images in Figure 7 show tomographic images of the static target achieved by processing the data relevant to Acquisition 1. Specifically, Figure 7a,b are the reconstructions in a local Cartesian reference system, while the bottom panels (Figure 7c,d) show the georeferenced reconstructions superimposed on a satellite image of the area. It turns out that both incoherent and coherent MIMO-MWT strategies provide consistent results with a peak in correspondence to the lighthouse's location. From a careful visual analysis, it can be seen that incoherent imaging results (left panels: Figure 7a,c) are characterized by superior focusing along the azimuth that is achieved through multiplicative image fusion operation. In the following, we tackle the imaging of the moving ship.

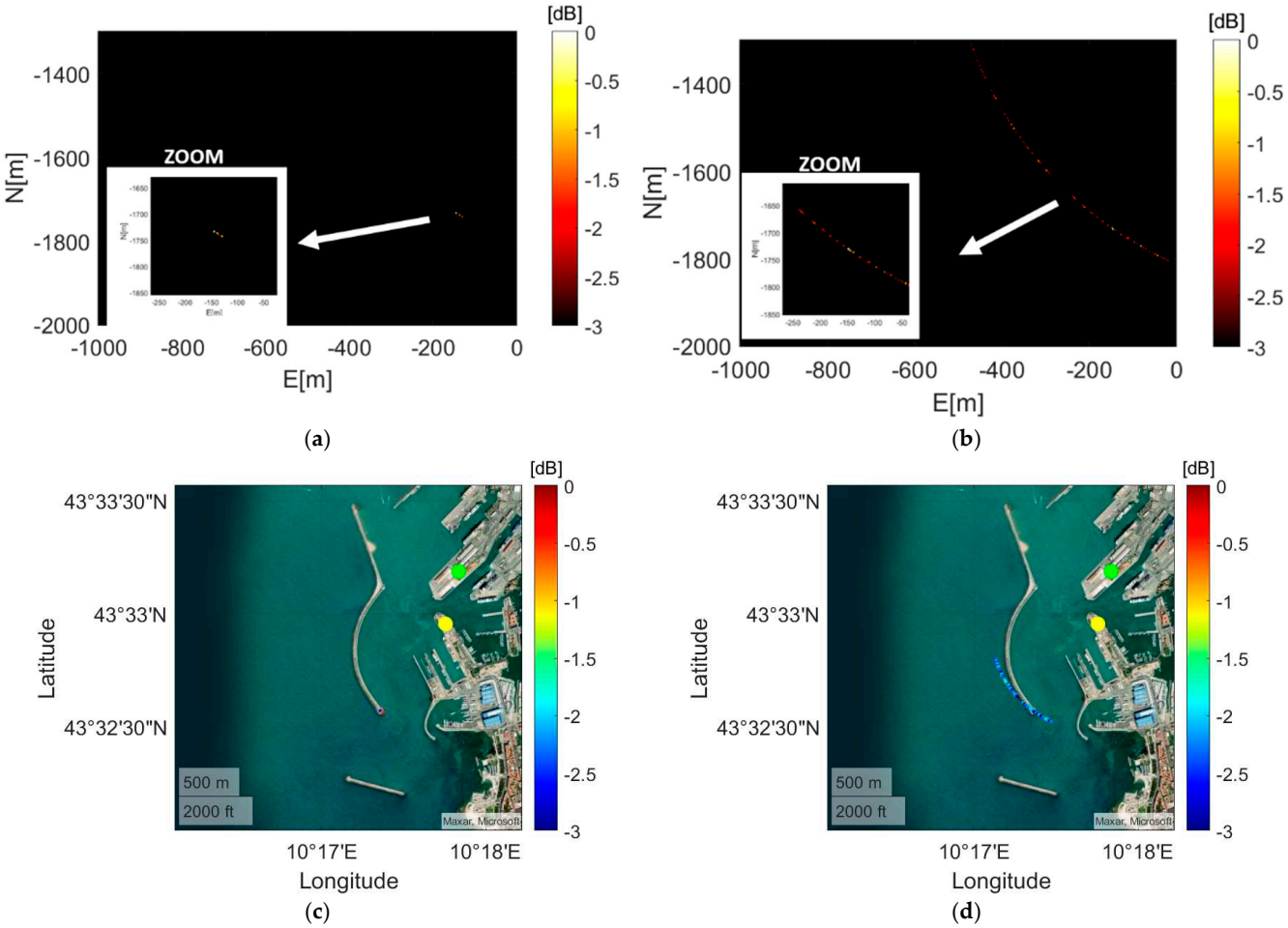

Figure 7. Tomographic reconstructions of the static target for Acquisition 1 in a local coordinate system (**a**,**b**) against a heat colormap scale with a [−3, 0] dB range. Reconstructions in a geographic coordinate system against a jet colormap scale with a [−3, 0] dB range (**c**,**d**). MIMO-MWT imaging results achieved through the MIMO-MWT-incoherent approach (left panel (**a**,**c**)) and MIMO-MWT-coherent approach (right panel (**b**,**d**)). The green and yellow dots represent the locations of the radar nodes RP1 and RP2, while the red circle denotes the location of the lighthouse.

Figure 8 shows zoomed-in sections of the RD map around the target of interest. Looking at the images, it emerges that, due to the spatial diversity, the channels are characterized by a different signal-to-noise ratio. Notably, the target signature is composed of multiple scatterers distributed along the range that move away from the sensors with a radial speed of approximately 2.5 m per second. These results are in agreement with the system's geometric parameters and the well-known route of the ship when it leaves the

port. Thanks to these distinctive features, data associated with the moving ship can be easily selected and processed by means of the MIMO-MWT focusing algorithms.

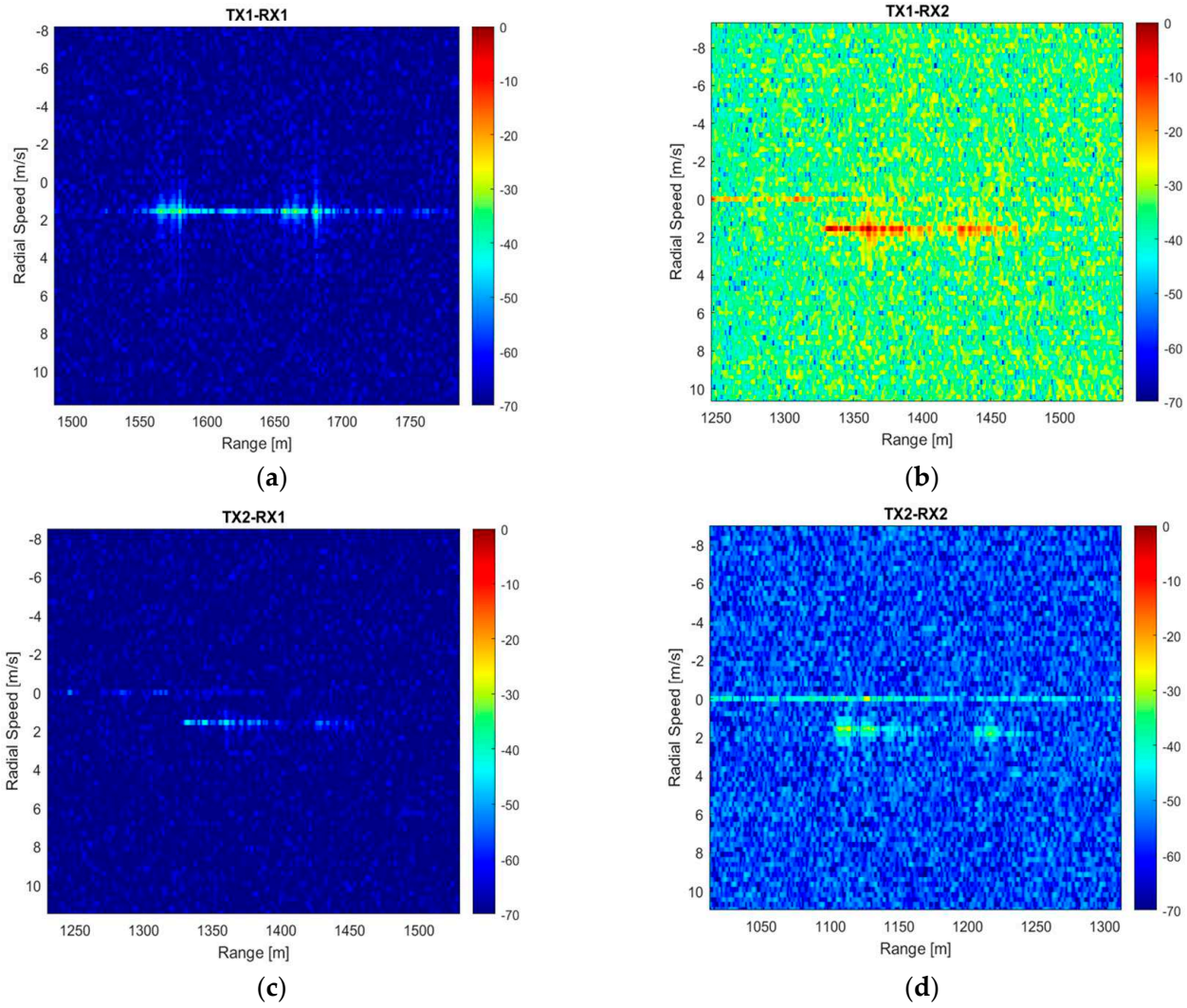

Figure 8. Zoomed-in sections of the RD map (normalized amplitude in dB) for each radar channel and Acquisition 1: RP1-RP1 (**a**), RP1-RP2 (**b**), RP2-RP1 (**c**), RP2-RP2 (**d**).

Figure 9 shows the imaging reconstructions for the monostatic (TX1-RX1, Figure 9a, and TX2-RX2, Figure 9d) and bistatic channels (TX1-RX2, Figure 9b, and TX2-RX1, Figure 9c) on the local east–north imaging plane, while the incoherent and coherent MIMO-MWT imaging results are depicted in Figure 9e,f. Owing to the measurement configuration, which causes a different backscattering from the target to the radar peripherals, the imaging results on the various channels look different. This behavior complies with the different target signatures previously observed in the range–Doppler maps of Figure 8. The reconstructions relevant to the single channels highlight that the system has a good range resolution (about 1.5 m) but a limited angular resolution due to the limited number of sensors and the large antenna beamwidth on the horizontal plane. The imaging reconstructions for both the coherent and incoherent approaches yield similar results; the target imaging contrast for the incoherent approach is better, as already shown for the static case.

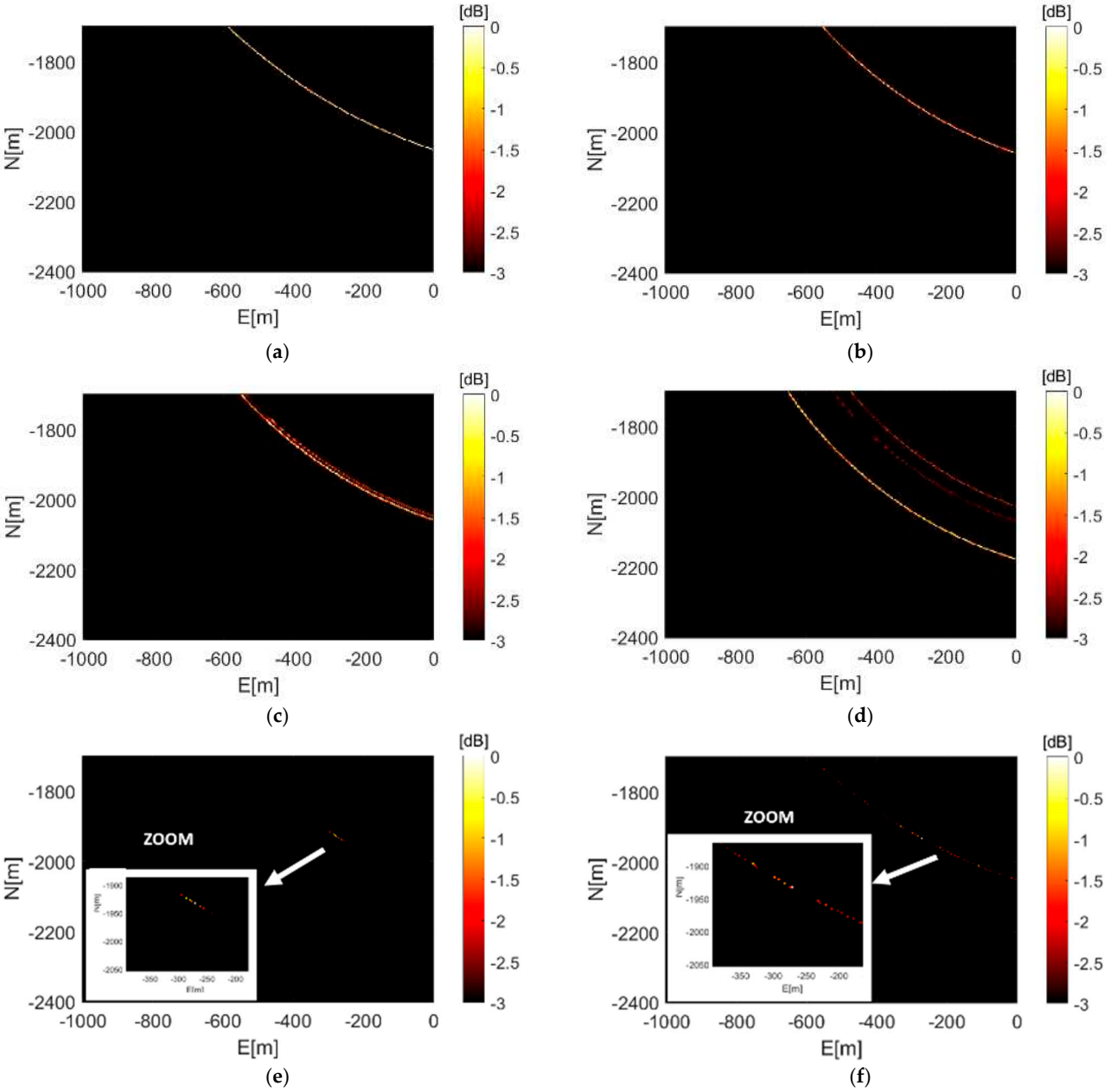

Figure 9. Imaging reconstruction by MIMO-MWT shown in a local coordinate system against a heat colormap scale with a [−3, 0] db range: channel TX1-RX1 (**a**); channel TX1-RX2 (**b**); channel TX2-RX1 (**c**); channel TX2-RX2 (**d**); MIMO incoherent imaging (**e**); MIMO coherent imaging (**f**).

Finally, we perform a time-varying analysis of the data frames recorded during the ferry's exit maneuver (see Table 2). Data collection was performed manually by the radar operator non-uniformly across time, thus leading to a non-uniform sampling of the target motion. This implies inhomogeneity in the imaging reconstruction process of the route followed by the target.

We report in Figures 10 and 11 all the georeferenced imaging reconstructions of the moving target for the incoherent and coherent imaging strategies, respectively. Again, the green and yellow dots represent the locations of two radar peripherals.

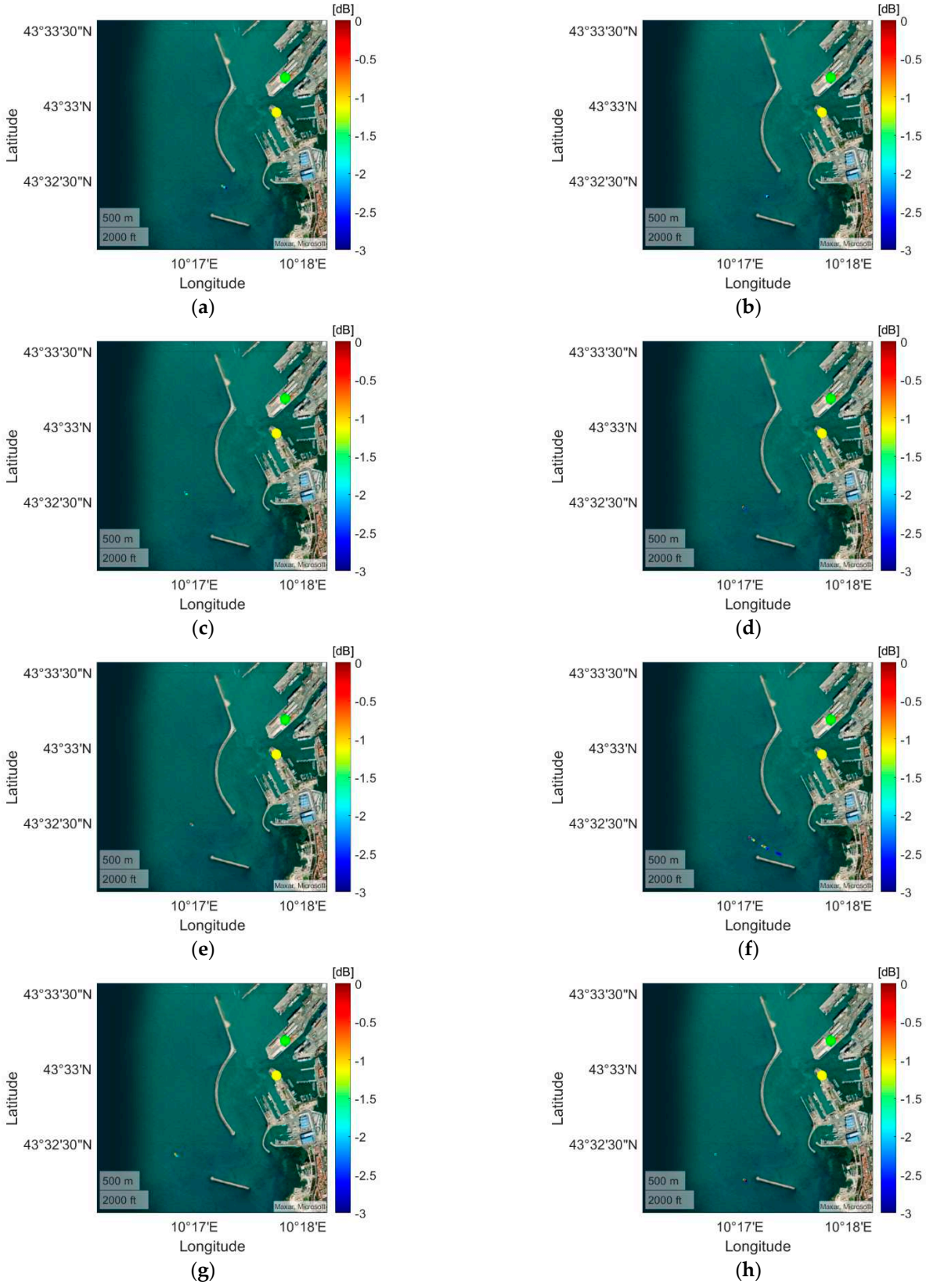

Figure 10. Georeferenced tomographic imaging reconstructions of the moving target for Acquisition frames 1–8 (**a**–**h**). These images were obtained using the MIMO-MWT-incoherent approach.

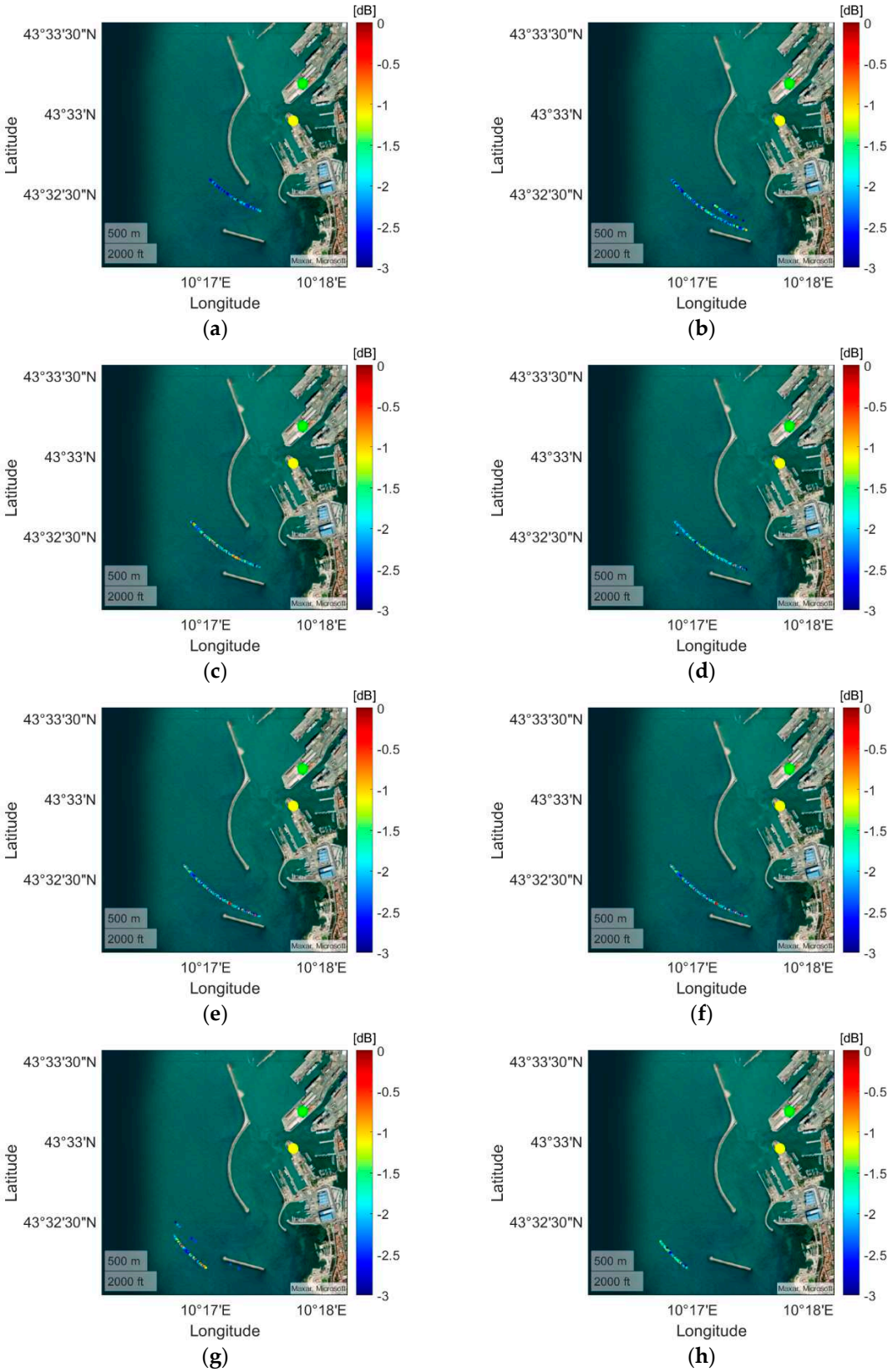

Figure 11. Georeferenced tomographic imaging reconstructions of the moving target for Acquisition frames 1–8 (**a**–**h**). These images were obtained using the MIMO-MWT coherent approach.

Both the coherent and incoherent approaches provide quite satisfactory imaging performance. However, coherent processing seems to provide a wider response along

the azimuth with respect to the incoherent approach, thus providing a lower accuracy on the exact localization of the target scatterers. In spite of this, the results depicted in Figures 10 and 11 suggest that both imaging approaches provide a good localization of the ferry during its navigation.

5. Discussion and Conclusions

The exploitation of microwave photonics has made feasible the centralized network paradigm for MIMO radars. The processing of raw data at a single central unit implies, in principle, no information loss during data fusion, and this was possible thanks to the inherent phase coherence ensured by the photonics-based approach for signal up- and down-conversion and distribution. Following the validation of a recently developed microwave photonics radar network prototype, we have proposed in this manuscript an advanced data processing approach based on microwave tomography for obtaining a focused image of the scene. Notably, coherent and incoherent focusing strategies have been developed and their preliminary experimental validation on both static and moving targets has been provided in a port environment.

Moreover, a multi-temporal analysis based on the imaging of multiple data frames referring to a Grimaldi Lines ferryboat has been conducted. The aim of the multi-temporal analysis was to assess the localization capabilities of the tomographic imaging algorithm. The target positions achieved through the imaging process have been compared with the nominal route typically taken by the ferryboat.

The encouraging achieved results motivate several future activities mainly devoted to overcoming the technical issues experienced regarding the use of the third radar peripheral as well as the X-band channels. The possibility of exploiting more channels operating at different frequency ranges will be investigated in order to ensure better coverage of the area under test and, at the same time, to take advantage of improved angular diversity and frequency diversity. Angular and frequency diversity, indeed, allow us to collect an increased amount of useful data, thus improving radar imaging capabilities. Therefore, improvements in the overall performance of photonic MIMO radar systems in terms of target localization and tracking can be expected following improvements of their hardware technology. Furthermore, we would like to note that the data frames were manually recorded by human operators; this could introduce delays and human errors in data collection. Accordingly, a possible future activity will rely on the development of an automatic procedure, capable of collecting multi-temporal data at constant intervals. These system improvements will open the possibility of developing innovative localization and tracking algorithms, thus allowing photonic MIMO radar technology to present itself as an effective solution in the context of maritime security.

Author Contributions: Conceptualization, C.N. and G.G.; methodology, all the authors; software and validation, C.N. and G.G.; formal analysis, C.N. and G.G.; data collection, S.M., A.M., F.S. (Filippo Scotti) and P.G.; writing—original draft, all the authors; revision, C.N., G.G., I.C. and S.M.; project administration, R.S. All authors have read and agreed to the published version of the manuscript.

Funding: This research received no external funding.

Data Availability Statement: The datasets presented in this article are not readily available because data are part of an ongoing study or due to technical limitations. Requests to access the datasets should be directed to antonio.malacarne@cnit.it.

Acknowledgments: This work was partially supported by the European Union under the Italian National Recovery and Resilience Plan (NRRP) of NextGenerationEU, partnership on "telecommunications of the future" (pe0000001—Program "RESTART").

Conflicts of Interest: The authors declare no conflicts of interest.

References

1. Li, J.; Stoica, P. *MIMO Radar Signal Processing*; John Wiley & Sons: New York, NY, USA, 2008.
2. O'Hagan, D.W.; Doughty, S.R.; Inggs, M.R. Chapter 5—Multistatic Radar Systems. In *Academic Press Library in Signal Processing, Volume 7: Array, Radar and Communications Engineering*; Chellappa, R., Theodoridis, S., Eds.; Elsevier: Amsterdam, The Netherlands; New York, NY, USA, 2018; pp. 253–275.
3. Li, J.; Stoica, P. MIMO Radar with Colocated Antennas. *IEEE Signal Process. Mag.* **2007**, *24*, 106–114. [CrossRef]
4. Haimovich, A.M.; Blum, R.S.; Cimini, L.J. MIMO Radar with Widely Separated Antennas. *IEEE Signal Process. Mag.* **2007**, *25*, 116–129. [CrossRef]
5. Skolnik, M.I. Introduction to Radar. *Radar Handb.* **1962**, *2*, 21.
6. Noviello, C.; Braca, P.; Maresca, S. Chapter 5—Radar Networks. In *Photonics for Radar Networks and Electronic Warfare Systems*; SciTech Publishing, Inc.: Raleigh, NC, USA, 2019; p. 111.
7. Wang, X.; Guo, Y.; Wen, F.; He, J.; Truong, T.K. EMVS-MIMO radar with sparse Rx geometry: Tensor modeling and 2D direction finding. *IEEE Trans. Aerosp. Electron. Syst.* **2023**, *59*, 8062–8075. [CrossRef]
8. Zhou, S.; Zang, H.; Wang, J.; Liu, H.; Xu, L.; Su, H. MIMO for conformal array radar: More than an option. In Proceedings of the 2015 IEEE Radar Conference, Johannesburg, South Africa, 27–30 October 2015; pp. 350–353.
9. Vasanelli, C.; Meinecke, B.; Mayer, J.; Elsayad, O.; Hügler, P.; Roos, F.; Zwick, T.; Waldschmidt, C. Characterization of mm-Wave Conformal Antenna Arrays for a 3×8 MIMO Radar. In Proceedings of the 2019 International Conference on Electromagnetics in Advanced Applications (ICEAA), Granada, Spain, 9–13 September 2019; pp. 0167–0171.
10. Wen, F.; Shi, J.; Lin, Y.; Gui, G.; Yuen, C.; Sari, H. Joint DOD and DOA Estimation for NLOS Target Using IRS-aided Bistatic MIMO Radar. *IEEE Trans. Veh. Technol.* **2024**, *73*, 15798–15802. [CrossRef]
11. Alhuwaimel, S.; Coetzee, S.; Cheng, P.; Du Plessis, D.; Fioranelli, F.; Griffiths, H.; Inggs, M.R.; Jordan, D.; Miceli, W.; O'Hagan, D.; et al. First Measurements with NeXtRAD, a Polarimetric X/L Band Radar Network. In Proceedings of the International Conference, IEEE Radar Conference (RadarConf), Seattle, WA, USA, 8–12 May 2017; pp. 1663–1668.
12. Inggs, M.R.; Lewis, S.; Palamà, R.; Ritchie, M.A.; Griffiths, H. Report on the 2018 Trials of the Multistatic NeXtRAD Dual Band Polarimetric Radar. In Proceedings of the 2019 IEEE Radar Conference (RadarConf), Boston, MA, USA, 22–26 April 2019.
13. Akcakaya, M.; Nehorai, A. MIMO radar detection under phase synchronization errors. In Proceedings of the 2010 IEEE International Conference on Acoustics, Speech and Signal Processing, Dallas, TX, USA, 14–19 March 2010; pp. 2578–2581.
14. Inggs, M.; Griffiths, H.; Fioranelli, F.; Ritchie, M.; Woodbridge, K. Multistatic Radar: System Requirements and Experimental Validation. In Proceedings of the 2014 International Radar Conference, Lille, France, 13–17 October 2014; pp. 1–6.
15. Sandenbergh, J.S.; Inggs, M.R. A Summary of the Results Achieved by the GPS Disciplined References of the NetRAD and NeXtRAD Multistatic Radars. In Proceedings of the 2019 IEEE Radar Conference (RadarConf), Boston, MA, USA, 22–26 April 2019.
16. Beasley, P.; Ritchie, M.; Griffiths, H.; Miceli, W.; Inggs, M.; Lewis, S.; Kahn, B. Multistatic Radar Measurements of UAVs at X-band and L-band. In Proceedings of the 2020 IEEE Radar Conference (RadarConf20), Florence, Italy, 21–25 September 2020; pp. 1–6.
17. Klare, J.; Saalmann, O. MIRA-CLE X: A New Imaging MIMO-Radar for Multi-Purpose Applications. In Proceedings of the 7th European Radar Conference, Paris, France, 30 September–1 October 2010; pp. 129–132.
18. Klare, J.; Biallawons, O.; Cerutti-Maori, D. UAV Detection with MIMO radar. In Proceedings of the 2017 18th International Radar Symposium (IRS), Prague, Czech Republic, 28–30 June 2017; pp. 1–8.
19. Tarchi, D.; Oliveri, F.; Sammartino, P.F. MIMO Radar and Ground-Based SAR Imaging Systems: Equivalent Approaches for Remote Sensing. *IEEE Trans. Geosci. Remote Sens.* **2013**, *51*, 425–435. [CrossRef]
20. Yang, F.; Qu, K.; Hao, M.; Liu, Q.; Chen, X.; Xu, F. Practical Investigation of a MIMO Radar System Capabilities for Small Drones Detection. *IET Radar Sonar Navig.* **2021**, *15*, 760–774. [CrossRef]
21. Serafino, G.; Maresca, S.; Di Mauro, L.; Tardo, A.; Cuillo, A.; Scotti, F.; Bogoni, A. A Photonics-Assisted Multi-Band MIMO Radar Network for the Port of the Future. *IEEE J. Sel. Top. Quantum Electron.* **2021**, *27*, 6000413. [CrossRef]
22. Pandey, G.; Scaffardi, M.; Maresca, S.; Amir, M.H.; Bogoni, A.; Malacarne, A. Coherent Multi-Band MIMO Radar: Robustness Analysis to SSMF-Based RF Signal Delivery. *Opt. Lett.* **2024**, *49*, 1528–1531. [CrossRef] [PubMed]
23. Karagiannidis, L.; Dres, D.; Protopapadakis, E.; Lamole, F.; Jacquin, F.; Rigal, G.; Ouzounoglou, E.; Katsaros, D.; Karalis, A.; Pierno, L.; et al. RANGER: Radars and Early Warning Technologies for Long Distance Maritime Surveillance. 2019. Available online: https://www.theseus.fi/handle/10024/266999 (accessed on 20 October 2024).
24. ROBORDER: Autonomous Swarm of Heterogeneous RObots for BORDER Surveillance. Available online: https://cordis.europa.eu/project/id/740593 (accessed on 20 October 2024).
25. Pastorino, M. *Microwave Imaging*; John Wiley & Sons: New York, NY, USA, 2010.
26. Noghanian, S.; Sabouni, A.; Desell, T.; Ashtari, A. *Microwave Tomography*; Springer: New York, NY, USA, 2014.
27. Maresca, S.; Serafino, G.; Noviello, C.; Scotti, F.; Fornaro, G.; Sansosti, E.; Ghelfi, P. Field Trial of a Coherent, Widely Distributed, Dual-Band Photonics-Based MIMO Radar with ISAR Imaging Capabilities. *IEEE J. Light. Technol.* **2022**, *40*, 6626–6635. [CrossRef]
28. Catapano, I.; Gennarelli, G.; Ludeno, G.; Noviello, C.; Esposito, G.; Soldovieri, F. Contactless Ground Penetrating Radar Imaging: State of the Art, Challenges, and Microwave Tomography-Based Data Processing. *IEEE Geosci. Remote Sens. Mag.* **2021**, *10*, 251–273. [CrossRef]

29. Gennarelli, G.; Soldovieri, F. A Linear Inverse Scattering Algorithm for Radar Imaging in Multipath Environments. *IEEE Geosci. Remote Sens. Lett.* **2013**, *10*, 1085–1089. [CrossRef]
30. Gennarelli, G.; Riccio, G.; Solimene, R.; Soldovieri, F. Radar Imaging Through a Building Corner. *IEEE Trans. Geosci. Remote Sens.* **2014**, *52*, 6750–6761. [CrossRef]
31. Catapano, I.; Gennarelli, G.; Esposito, G.; Ludeno, G.; Su, Y.; Zhang, Z.; Soldovieri, F. Contactless Microwave Tomography via MIMO GPR. *IEEE Geosci. Remote Sens. Lett.* **2023**, *20*, 3502505. [CrossRef]
32. Chew, W.C. *Waves and Fields in Inhomogeneous Media*; Institute of Electrical and Electronics Engineers: Piscataway, NJ, USA, 1995.
33. Bertero, M.; Boccacci, P. *Introduction to Inverse Problems in Imaging*; Institute of Physics Publishing: Bristol, UK; Philadelphia, PA, USA, 1998.
34. Hansen, P.C. *Discrete Inverse Problems: Insight and Algorithms*; Society for Industrial and Applied Mathematics: Philadelphia, PA, USA, 2010.
35. Richards, M.A.; Sheer, L.; Holm, W.A. *Principles of Modern Radar*; SciTech Publishing, Inc.: Raleigh, NC, USA, 2010.
36. Noviello, C.; Fornaro, G.; Martorella, M. Focused SAR Image Formation of Moving Targets Based on Doppler Parameter Estimation. *IEEE Trans. Geosci. Remote Sens.* **2015**, *53*, 3460–3470. [CrossRef]
37. Gennarelli, G.; Vivone, G.; Braca, P.; Soldovieri, F.; Amin, M.G. Comparative Analysis of two Approaches for Multipath Ghost Suppression in Radar Imaging. *IEEE Geosci. Remote Sens. Lett.* **2016**, *13*, 1226–1230. [CrossRef]

Disclaimer/Publisher's Note: The statements, opinions and data contained in all publications are solely those of the individual author(s) and contributor(s) and not of MDPI and/or the editor(s). MDPI and/or the editor(s) disclaim responsibility for any injury to people or property resulting from any ideas, methods, instructions or products referred to in the content.